Pediatric Radiology
https://doi.org/10.1007/s00247-024-06014-3

ESPR 2024, SEVILLE

Pediatric forensic postmortem computed tomography: basics to advanced

Sharon W. Gould[1] · **Mary Harty**[1]

Received: 2 May 2024 / Revised: 18 July 2024 / Accepted: 22 July 2024

Abstract
The approach to postmortem computed tomography (CT) differs significantly from that of diagnostic CT in living patients. Elimination of artifacts such as noise and beam hardening as well as optimization of tissue contrast requires alteration of exposure parameters from protocols designed to limit radiation dose in children. Multiple scans may be performed, and detailed post-processing can be used to enhance subtle findings such as small intracranial extra axial collections and non-displaced fractures. Basics of postmortem CT technique are discussed here as well as advanced techniques in scanning and post-processing.

Keywords Computed tomography · Forensic · Pediatric · Postmortem

Introduction

Scanning technique for unenhanced forensic pediatric postmortem computed tomography (PMCT) should be designed to identify bone, soft tissue, and lung pathology; to detect hemorrhage and foreign bodies; and possibly even to aid in identification of remains and determination of cause of death. There are a number of reports that describe ways to optimize postmortem CT technique [1–5]. It is important to remember that the As-Low-As-Reasonably-Achievable (ALARA) principle applied to routine clinical imaging does not apply in the postmortem setting [1]. Strategies for the selection of imaging protocols discussed below incorporate parameters designed to reduce noise, improve spatial resolution, and reduce beam hardening artifact when necessary [1, 3, 6] in order to provide very high-resolution images to identify injuries or other pathology that may help differentiate suspected physical abuse from sudden unexplained infant death (SUDI), find undiagnosed pathology, or even disclose unknown congenital anomalies. Because the imaging data from these studies may be used to contribute to conviction or dismissal of a manslaughter charge, protect the pediatric siblings of the deceased, or form the basis of family counseling, even with regard to future pregnancies, attention to detail is paramount, and higher dose scans can be utilized to have the best opportunity for detection of abnormalities. Basic principles will be discussed here as well as an overview of newer techniques including dual-energy CT (DECT), ventilated PMCT, and postmortem CT angiography (PMCTA) with a brief discussion of post-processing options.

Basic technique

Optimization of image quality requires selection of scan protocol parameters for high tissue contrast, high spatial resolution, and minimal noise (Fig. 1). Tissue contrast varies with the beam energy (kVp) and tissue properties, and the scan kVp should be chosen accordingly, usually 120 kVp to balance noise, potential beam hardening, and tissue contrast [1, 4, 7]. Because postmortem scans are commonly performed without intravenous contrast material, attention to intrinsic soft tissue contrast is important. An additional consideration is metallic implants or foreign bodies that may create streak artifact with a lower beam energy. For example, supportive lines and tubes placed during resuscitative efforts should be left in place during at least the first scan for documentation of placement as well as to identify associated changes in the surrounding

---

✉ Sharon W. Gould
sgould@nemours.org

Mary Harty
Mary.Harty@nemours.org

[1] Radiology Department, Nemours Children's Health DE, 1600 Rockland Road, Wilmington, DE 19803, USA

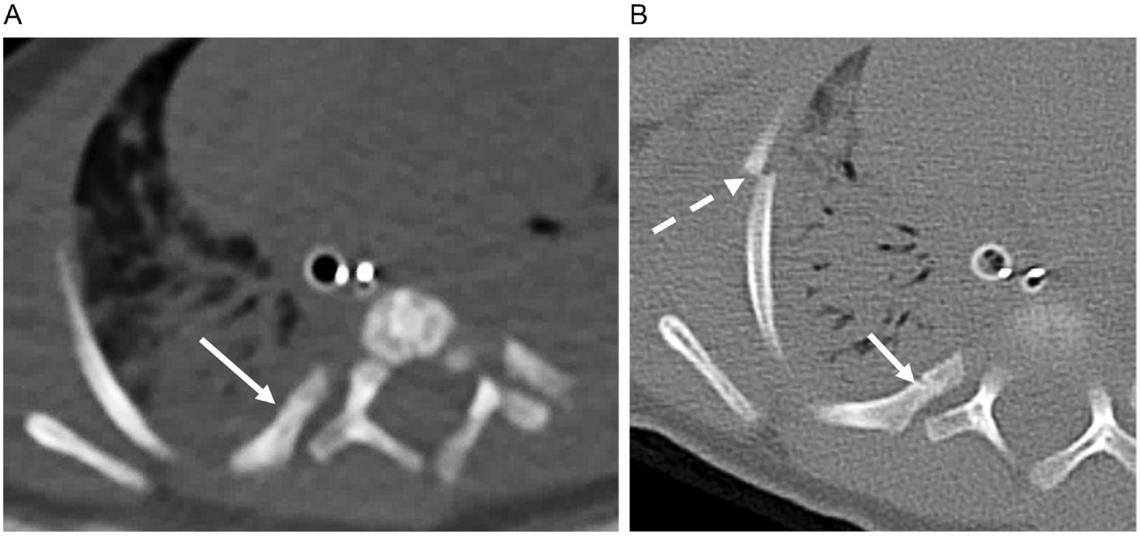

Fig. 1 A 2-month-old boy who was a victim of physical abuse. **a** An axial antemortem computed tomography (CT) scan performed with low-dose technique, 80 kVp beam energy, and a tube current of 190 mA with a pitch of 0.8, a 200-mm field of view (FOV), and a soft tissue kernel has poor resolution for bone assessment. A posterior rib fracture is obscured (*arrow*). **b** An axial image from the postmortem CT performed later the same day with higher dose technique, 120 kVp, and a pitch of 0.6, a sharp kernel, and a 190-mm FOV reveals the posterior rib fracture (*arrow*). A displaced right lateral rib fracture is also visible (*broken arrow*). The tube current for the postmortem CT was 65 mA, lower than desirable because tube current modulation was mistakenly left on

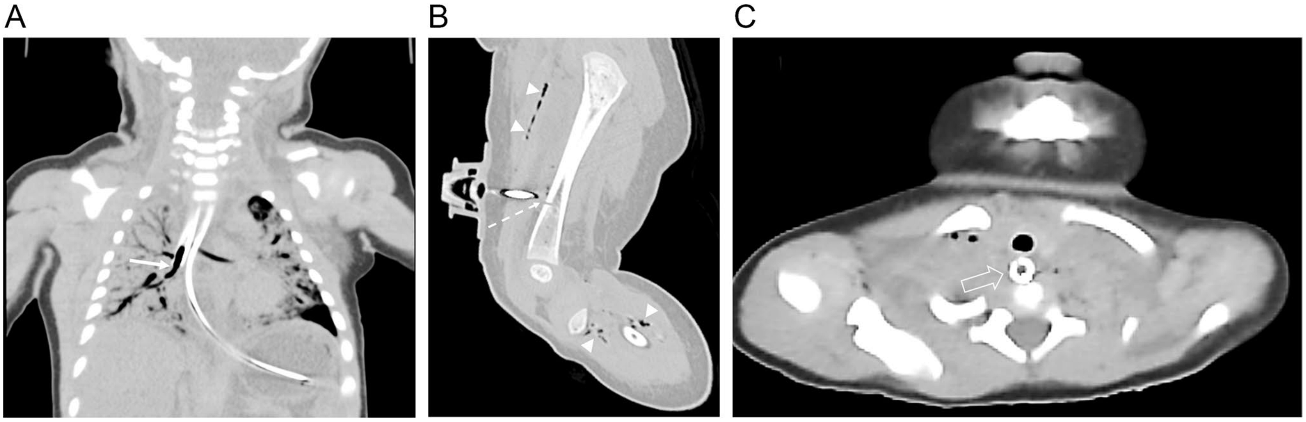

Fig. 2 Postmortem computed tomography should include images with support devices in place both for helping to correlate with any local tissue changes found on autopsy that may result from device placement and for training and feedback. **a, b** A 2-month-old boy who was a victim of inflicted injury. **a** A coronal reformatted image of the chest shows the endotracheal tube tip to be in the right bronchus intermedius (*arrow*). **b** A sagittal reformatted image of the left femur shows an intraosseous needle with its tip in the anterior soft tissues. There is a round defect in the anterior femoral diaphyseal cortex (*broken arrow*) where the needle pierced the bone. The extent of soft tissue emphysema (*arrowheads*) suggests that fluid was administered while the needle tip was displaced from the bone. **c** Axial chest image in a 2-month-old girl with unexplained death. The endotracheal tube was placed in the esophagus (*arrow*) during resuscitation attempts

tissues [8] (Fig. 2); however, beam hardening from these devices can be an issue at lower beam energies. Reduced radiation dose is not a consideration in postmortem imaging and additional scans can be performed at a higher kVp setting to reduce beam hardening artifact as soft tissue contrast will be better demonstrated on the lower beam energy acquisition.

The reconstruction algorithm or kernel can be selected to emphasize different tissue characteristics, as well as alter noise appearance. For example, in creating a lung series, a moderately sharp contrast or even edge enhancement kernel may be selected to highlight fine detail (Fig. 3). A very sharp kernel may be useful for bone images but will result in increased noise artifact [2]. A smoother algorithm associated

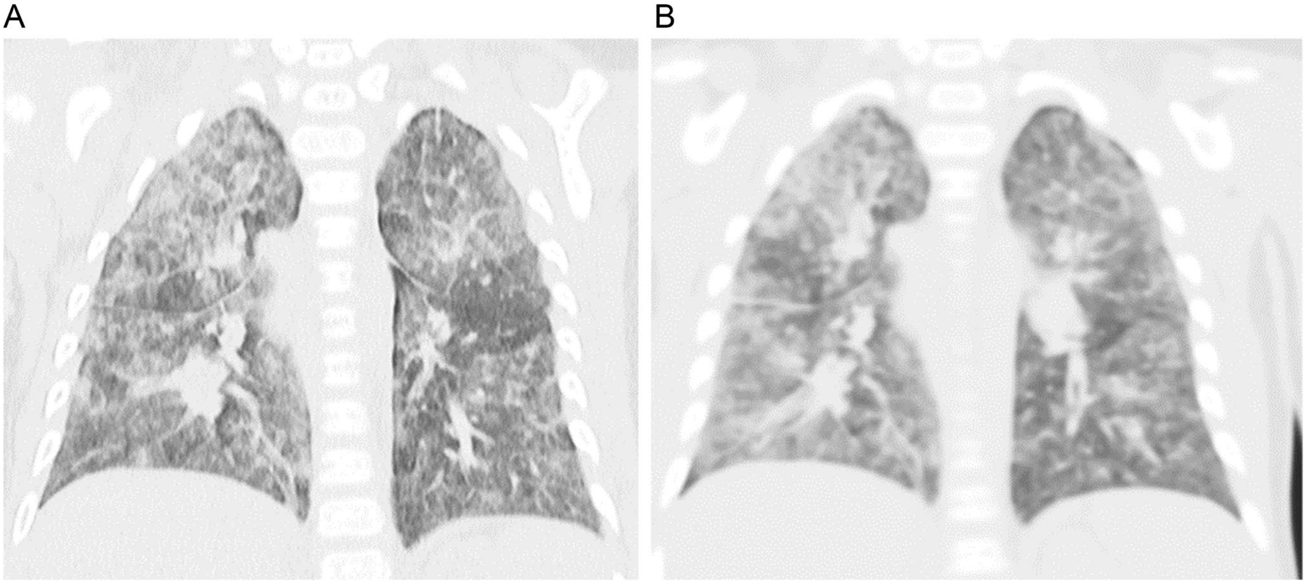

Fig. 3 **A** 7-month-old boy who was found unresponsive and wedged between the bed and the wall. **a** A coronal reformatted image constructed with a very sharp kernel demonstrates pulmonary interstitial and vascular detail. **b** A coronal reformatted image from the same acquisition with a soft kernel has poorer spatial resolution with indistinct pulmonary markings

with decreased noise would be appropriate for brain and soft tissue viewing [1, 3, 4] (Fig. 4) as well as for reconstruction of data to be used to render 3-D (dimensional) images [3].

Spatial resolution will depend upon scanner type and detectors as well as scanning field of view (FOV), reconstructed FOV, matrix size, and slice reconstruction parameters and is influenced by noise and contrast. Helical, multidetector scanners are ideal for postmortem scanning [3] as they provide narrow detector collimation for small, reconstructed voxel size providing high spatial resolution [9] and eliminate artifact from axial scans (Fig. 5). Collimation width for pediatric PMCT is recommended to be less than 1 mm [1, 4, 5, 10, 11]. The rotations can be set to overlap resulting in a pitch of less than one, meaning the table moves less than the detector width for each 360° gantry rotation [1, 2, 4]. The overlap created by a low pitch prevents artifacts related to required data interpolation for a high pitch where the table moves more than the detector

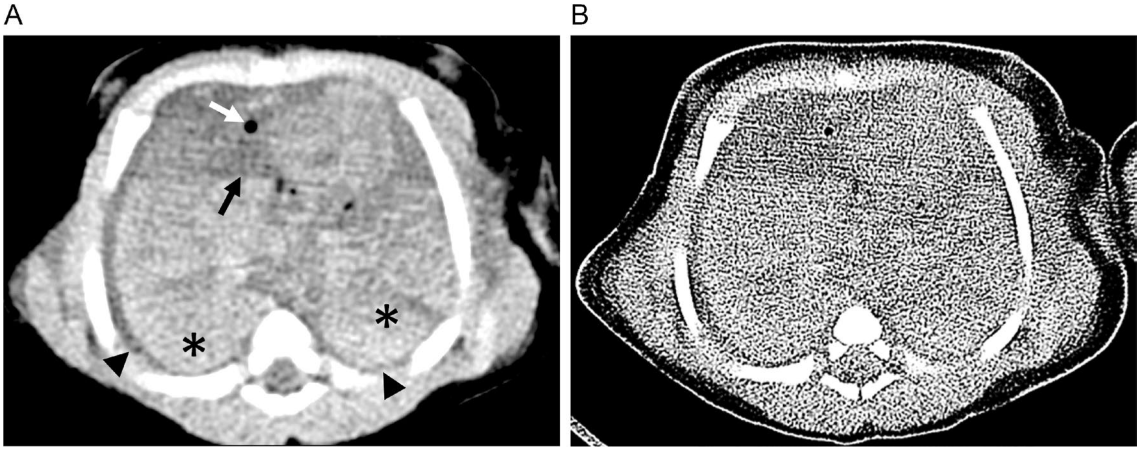

Fig. 4 A 9-day-old girl who presented to the primary physician apneic and pulseless and who underwent prolonged resuscitation efforts during multiple hospital transfers. **a** An axial image of the lower chest constructed with a smooth, soft tissue kernel and displayed with a soft tissue window shows completely airless lungs (*asterisks*) with bilateral pleural effusions (*arrowheads*), layering blood products in the right atrium (*black arrow*), and intracardiac gas (*white arrow*). **b** The same axial slice from the same acquisition constructed with a high contrast sharp kernel accentuates image noise and obscures soft tissue detail when viewed with a soft tissue window

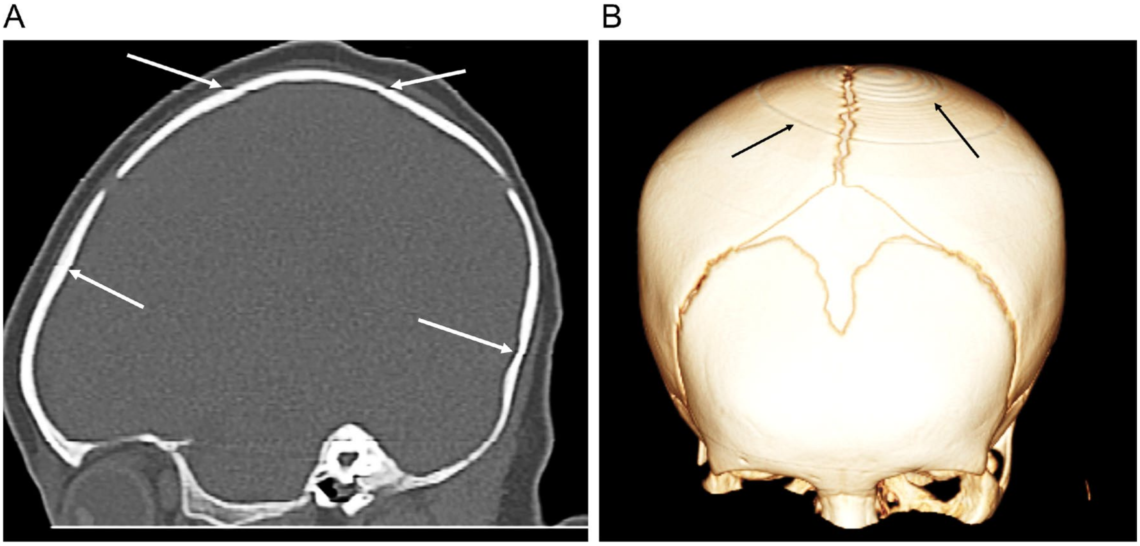

Fig. 5 A 4-month-old girl with sudden unexplained death. **a** A sagittal reformatted image shows linear artifacts throughout the scan that are most noticeable in the calvarium (*white arrows*). These artifacts are associated with axial scan acquisition. **b** A volume rendered image viewing the calvarium from an anterosuperior perspective shows these artifacts as concentric circles (*black arrows*)

width for each gantry rotation. Both the overlapping exposure and a slow gantry rotation time of 1 s [2, 11] result in a higher effective tube current over the course of the scan, reducing noise and improving spatial resolution (Fig. 6).

Scanning FOV should be as small as patient body habitus and positioning allow to provide maximal spatial resolution. While some authors advocate a single scan of the whole body [5], others recommend scanning the head and

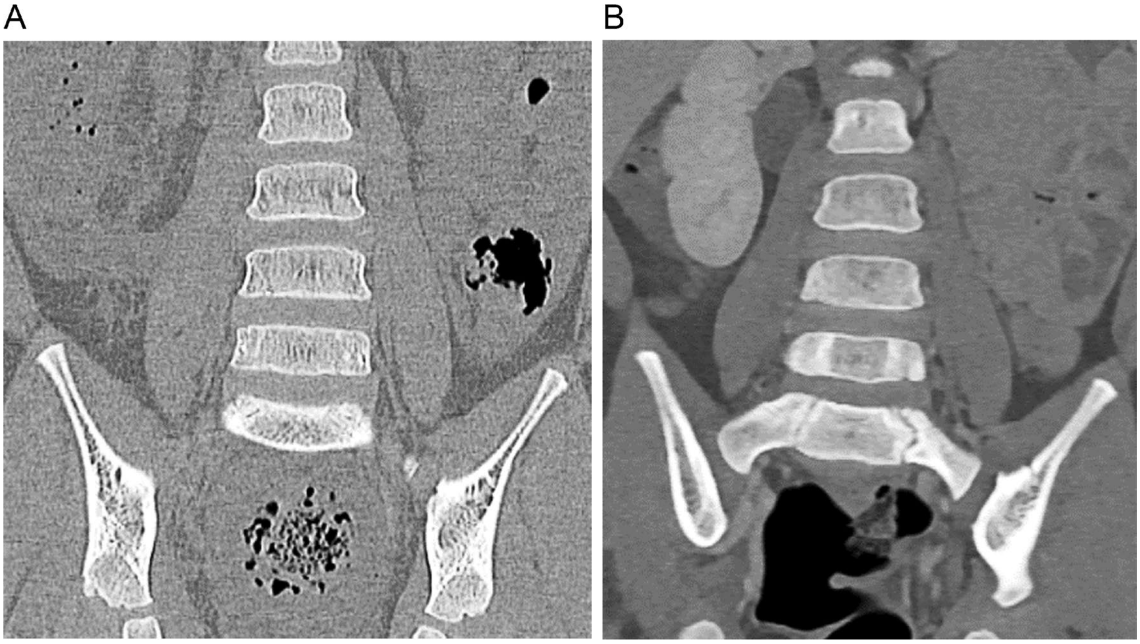

Fig. 6 A 5-year-old boy who died following a motor vehicle accident. **a** A coronal reformatted image of the lumbar spine shows vertebral trabecular detail. This scan was obtained with a pitch of 0.4 and high dose technique: 120 kVp, 384 mA, computed tomography dose index per volume (CTDIvol) of 26.37 mGy. **b** A coronal reformatted image of the lumbar region of this same child was obtained during a high-pitch (3.4), low-dose (kV 100, mA 850, CTDIvol 2.93 mGy) scan performed 2 years earlier for abdominal pain. The bone detail is much less apparent even though both scans were obtained with the same detector collimation (0.6 mm) and have the same reconstruction kernel and window

neck and extremities with a smaller FOV in addition to a whole-body scan with a larger FOV to accommodate the body [1, 4], the latter technique is suitable for larger patients. The reconstructed FOV can be a different diameter from the scanned FOV. A smaller reconstructed FOV can be created from raw data to effectively assign less area to the XY (axial plane) matrix and decrease voxel size with increased in-plane resolution [2] (Fig. 7). The smaller FOV can be created off-center and is valuable for detailed evaluation of small parts such as facial bones, and extremities. Some scanners also permit reconstruction of an extended FOV for imaging of body parts not included within the standard FOV for large patients or patients with rigor mortis whose extremities may be fixed outside the scan. Caution regarding assessment of attenuation is needed as the Hounsfield units may vary outside the standard diameter [12].

Slice thickness reconstructions for image viewing will vary with patient size and region of interest [3]. For example, thinner slices may be desirable for facial bones, but unnecessary for abdominal soft tissues. In clinical, low-dose scanning, the increased noise associated with thin slice reconstructions may limit utility for viewing, but with the higher doses used for PMCT, thin slices may be desirable for decreased voxel size to limit volume averaging and windmill artifact [13]. Thin, sub-millimeter slices are best for artifact-free multiplanar reconstructions (MPRs), volume rendered (VR) images, and storage in the event of later requests for additional reconstructions. Data can be reconstructed with an overlap permitting reconstruction of isometric voxels for optimal multiplanar reformatting and 3-D rendering without artifact [9, 14] (Fig. 8). Slice thickness cannot be reconstructed thinner than detector width, however, and so a narrow detector width is imperative.

Image noise directly affects both tissue contrast and spatial resolution. For PMCT, increasing the tube current above settings utilized in clinical scanning is an important strategy to minimize noise and improve both tissue contrast and spatial resolution (Figs. 1, 9, 10). To avoid an insufficient exposure, most authors recommend a fixed tube current [1, 4, 5] (Table 1). As discussed above, a narrow detector width is ideal for high spatial resolution, but the smaller detectors receive fewer photons which increases noise. By increasing tube current over clinical scan parameters, the noise associated with tight collimation is reduced. Iterative reconstruction is utilized in clinical imaging for noise reduction to allow decreased radiation dose. In PMCT, however, this strategy should be used with caution due to the potential for loss of detail and spatial resolution with a strong algorithm [2], particularly in assessment of subtle fractures.

Image reconstruction

Once scanning is complete, image reconstruction for viewing will be performed based on the needs of the specific case (Table 2). As discussed above, slice reconstruction for axial images and MPRs is performed with the slice thickness, kernel, degree of iterative reconstruction appropriate for body part, and tissue visualization (Fig. 11). Isometric voxels are required for smooth reconstructions performed in non-axial planes with overlapping slice data preferred to eliminate stair-step artifact [2, 4, 14, 15] (Figs. 11 and 12). For best viewing of high-resolution detail, such as temporal bone, lung parenchyma, or long bone metaphyses, reconstructions utilizing thin slices with a sharp kernel and a small reconstructed FOV will help improve spatial resolution. In addition to routine coronal and sagittal plane images, utilization

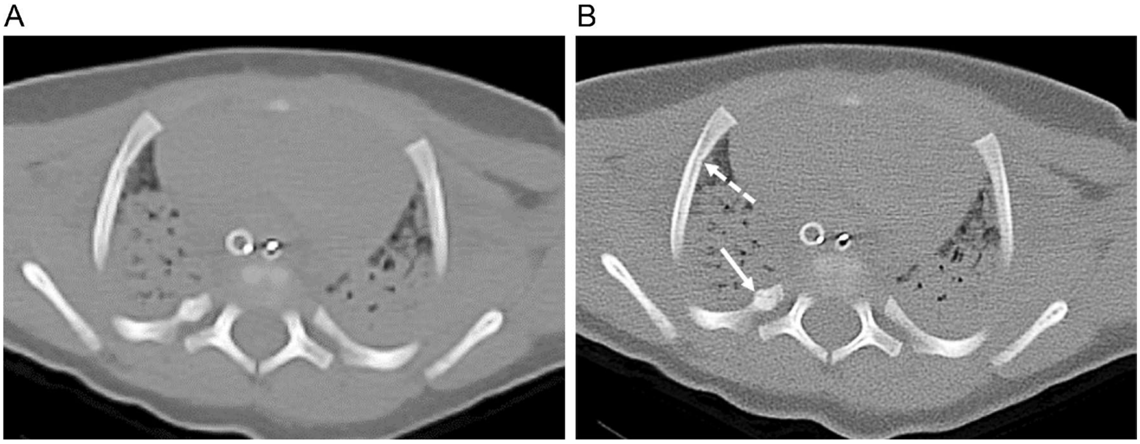

Fig. 7 A 2-month-old boy who was a victim of known physical abuse. **a** A 2-mm-thick axial image with a soft kernel and a 413-mm reconstructed field of view shows little bone detail. **b** The same 2-mm axial slice from the same acquisition with a reconstructed field of view of 190 mm and a sharp kernel shows much more detail permitting identification of the healing posterior right rib fracture (*white arrow*), and the CPR-related buckle fracture of the lateral right rib (*broken arrow*)

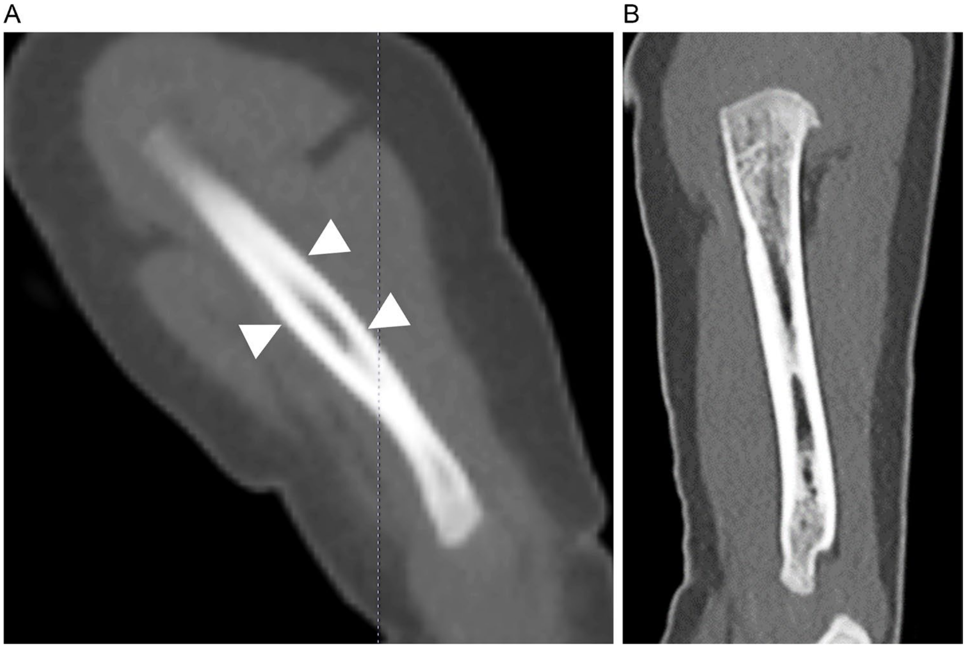

Fig. 8 **a** A 4-month-old girl with sudden unexplained death. A sagittal reformatted image that is oblique to the long axis of the right humerus shows step artifact that blurs the bone cortex. The reformatted image was derived from 1.5-mm slices without overlap, leading to the step artifact (*arrowheads*). **b** A 10-week-old girl (a different patient) with unexplained death. A sagittal reformatted image of the right humerus derived from 0.6-mm slices with an overlap of 0.2 mm has a clear and smooth appearance of the humeral cortex without step artifact

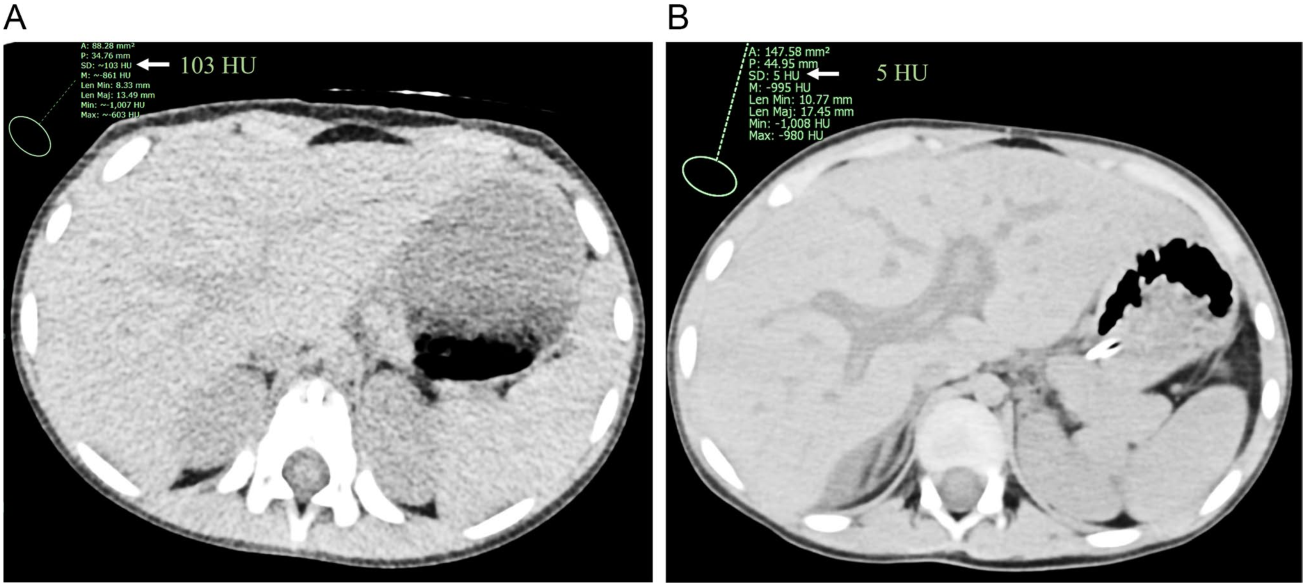

Fig. 9 **a** A 3-year-old living boy with suspected renal calculi. This scan was performed with dose reduction technique: 100 kVp, 65 mA, pitch 0.8, dose modulation on. The standard deviation of the Hounsfield units (HU) in air provides a reasonable estimation of image noise and in this case was 103 HU. There is a mottled appearance of the soft tissues on this axial unenhanced image. **b** A 3-year-old deceased boy (a different patient) who died after suspected accidental drowning. This axial image was performed with high-dose technique: 120 kV, 384 mA, pitch 0.4 with no dose modulation. There is little mottling of the soft tissues and an HU standard deviation in air of 5, indicating much less image noise

of planes along the axes of the structure being evaluated, i.e., parallel to a long bone axis/perpendicular to the physis in the setting of potential metaphyseal lesions [4] (Fig. 13) or oblique, angled, or curved reconstruction along the ribs [14, 16], will aid in detection of pathology (Fig. 14). An extended Hounsfield unit scale is available for reconstruction on some scanners to aid in assessment of highly radiopaque structures [2], which can be viewed with reconstructed planes oriented to the object, or with a maximum intensity projection series. X-ray-like reconstructions consisting of large-volume MPR images or summated data that can simulate oral pan tomograms [8, 14, 17] may be useful in some circumstances. As discussed above, reconstructed, overlapping thin slice data with a smooth kernel should be utilized for 3-D volume

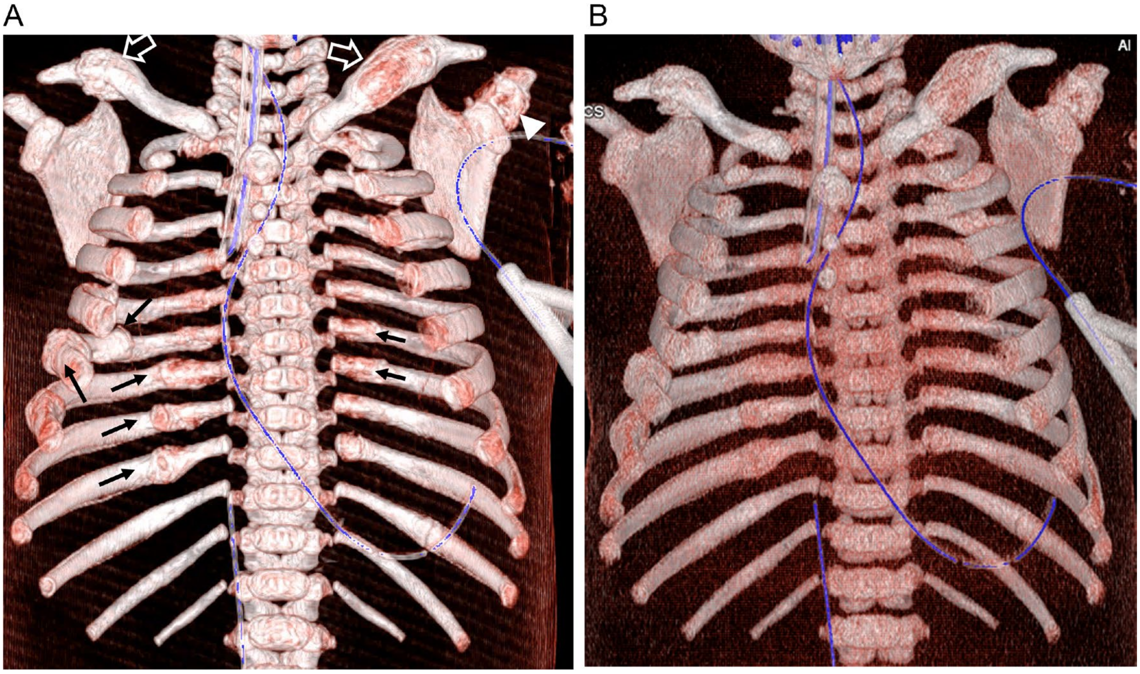

Fig. 10 An 80-day-old boy with unexplained death with evidence of extensive fractures compatible with physical abuse at postmortem imaging. **a** A frontal view volume rendered image of the thoracic cage constructed from a scan with a tube current of 365 mA shows numerous rib fractures with healing response (*arrows*) as well as healing bilateral clavicular fractures (*open arrows*) and a partially healed left scapular fracture (*arrowhead*). **b** A frontal view volume rendered image reconstructed from a scan performed at the same time but with a tube current of 65 mA has so much noise artifact that the rib fractures are harder to see. Both scans were performed at 120 kV. Increasing tube current for postmortem imaging is crucial for noise reduction

rendering or cinematic rendering to eliminate stair-step artifacts and improve detection of surface abnormalities (Fig. 12). These types of reconstruction are highly useful for detection of linear, non-depressed skull fractures [18] and skeletal dysplasias [19] (Fig. 15). Cinematic rendering (Syngo Via, Siemens Healthineers, Erlangen, Germany) is a newer post-processing technology that provides more photorealistic, detailed 3-D images through utilization of information from high dynamic range rendering light maps. This process provides more natural illumination and more predicted photon scattering patterns resulting in improved depth and shape perception due to improved depiction of reflections and shadowing [19–21]. Cinematic rendering offers improved depiction of bone or surface abnormalities such as soft tissue lacerations or skeletal dysplasias [21] (Fig. 15).

Advanced techniques

Spectral decomposition performed through dual-energy scanning or photon counting can provide improved soft tissue contrast by utilizing the different attenuation values of different elements at different beam energies. For example, even without iodinated contrast, this technique can be used to select and subtract voxels with calcium to subtract bone, a useful technique to improve visibility of small extra axial hemorrhages in the head [22–24] (Fig. 16). Imaging at more than one beam energy also creates the opportunity to reconstruct the data as though the scan was performed at a selected virtual beam energy. A lower beam energy improves soft tissue contrast but may suffer from increased noise (Fig. 17). A higher beam energy will decrease beam hardening, for example, at the pons or adjacent to a metal object, but soft tissue characteristics may be diminished [22, 23]. The blend of data from the high and low kilovolt (kV) tubes can be adjusted for noise and beam hardening artifact, but as with virtual mono kiloelectron volt (keV) reconstructions, will alter soft tissue contrast. For optimal spectral separation, the beam energies should be as different as possible. For dual-energy scanning, 80 and 140 kV are most often utilized, unless the patient is very large [2, 4, 22].

Postmortem CTA has been reported as a method of imaging opacified vessels and tissues to overcome the limitations of routine PMCT in which analysis of soft tissue structures is limited [25–27]. Increased vascular permeability postmortem limits the utility of routinely used water-soluble contrast media in adult-sized patients [26–28]. To overcome this phenomenon, use of water-soluble contrast in polyethylene glycol [29, 30] has been reported. This technique provides

Table 1 Recommended technique for pediatric postmortem computed tomography

Body part	Age	Range	Study								
			Gould et al. [4]					Shelmerdine et al. [5]			
			kVp	Eff[a] mAs	Ref mA[b]	Pitch	FOV[c] (Maximum)	kVp	mAs	Pitch	FOV[c]
Whole body	General (Gould et al.: 5 + years)	Head to pelvis	120	480		0.7	Up to 500	120	200–299	0.5–0.8	Adjusted
	9 months-5 yrs	Head – pelvis	120	480		0.7	320				
	< 9 months	Ears – toes	120	480		0.7	320				
Head/neck	General (5 + years)	Vertex to carina	80/140 (Dual energy)		290	0.7	160				
	9 months-5 years	Vertex to carina	80/140 (Dual energy)		264	0.7	160				
	< 9 months	Vertex to sacrum	80/140 (Dual energy)		264	0.6	160				
Extremities	> 5 years	Pelvis to toes	140	400		0.4	Up to 500				
	< 5 years	Pelvis to toes	120	480		0.4	320				
	All	Each upper extremity separately	120	480		0.4	320				
	Large patients	Lower extremities individually if needed	120	480		0.4	As needed				

[a] Eff mAs is the tube current/time product that the scanner will meet over the time duration of the scan

[b] Ref mA is utilized with dual source dual energy scanning. The tube current for each tube will adjust for a similar degree of noise

[c] FOV in this table refers to scanning field of view and should be adjusted to be as small as possible while still including the entire patient

Eff mAs effective milliampere-seconds, *FOV* field of view, *kVp* kilovoltage peak, *mAs* milliampere-seconds, *Ref mAs* reference milliampere-seconds

Table 2 Recommended reconstructions for pediatric postmortem computed tomography

Body part	Age	Range	Kernel/filter	Planes	Slice thickness (mm)	Window	3DVR
Whole body	< 1 year	Vertex to toes	Soft tissue/soft	Axial	0.625	Soft tissue	As needed
				Coronal	3	Soft tissue	
				Sagittal	3	Soft tissue	
	> 1 year	Vertex to pelvis	Soft tissue/soft	Axial	0.625	Soft tissue	As needed
				Coronal	5	Soft tissue	
				Sagittal	5	Soft tissue	
Head and neck	All	Vertex to carina	Soft tissue/soft	Axial	3	Brain	Skull flip and rotate without the C-spine
				Coronal			
				Sagittal			
			Bone/sharp	Axial	3	Bone	
				Coronal			
				Sagittal			
Trunk	< 1 year	Ears to pelvis	Soft tissue/soft	Axial	3	Soft tissue	Rib cage flip and rotate Pelvis flip and rotate as needed
				Coronal			
				Sagittal			
			Bone/sharp	Axial	3	Bone	
				Coronal			
				Sagittal			
			Lung/medium sharp	Axial	2	Lung	
	> 1 year	Ears to pelvis	Soft tissue/soft	Axial	5	Soft tissue	Rib cage flip and rotate Pelvis flip and rotate as needed
				Coronal			
				Sagittal			
			Bone/sharp	Axial	5	Bone	
				Coronal			
				Sagittal			
			Lung/medium sharp	Axial	2	Lung	
Spine	All	Skull base to coccyx	Bone/sharp	Axial – angled if needed	2	Bone	Whole spine flip and rotate
				Sagittal	2		

Table 2 (continued)

Body part	Age	Range	Kernel/filter	Planes	Slice thickness (mm)	Window	3DVR
Extremities-Upper extremities should be performed as separate scans for each arm	< 1 year	Shoulder-finger tips/Acetabular roof -toes. Both legs together	Bone/sharp[a]	Axial of each arm/axial both legs together	3	Bone	Flip and rotate of each humerus, forearm and hand, femur, and lower leg and foot should be performed separately. These may be best if created from data constructed with a soft tissue rather than a bone kernel
				Coronal to long bone for each side, separate humerus, forearm, femur, and tibial reconstructions	3		
	> 1 year	Shoulder-finger tips/Acetabular roof -toes. Legs can be scanned separately for large patients	Bone/Sharp[a]	Axial of each arm/axial of each leg	5	Bone	
				Coronal[b] to long bone for each side, separate humerus, forearm, femur, and tibial reconstructions	5		

[a] Additional soft kernel reconstructions can be performed if needed

[b] Sagittal reconstructions can be performed in addition as needed

3-DVR 3-dimensional volume rendering, *C-spine* cervical spine

myocardial, abdominal organ, and some tumor enhancement [30] with differentiation of arterial and venous phases possible due to a decrease in vascular enhancement over 15–20 min [31]. Use of oil-based contrast mixed in oil has also been described [27, 28, 32] with persistence of vascular enhancement up to 72 h [30]. Extravasation of oil-based contrast into the pancreas and gastric mucosa has been reported and may simulate pathology [28, 32]. Administration of contrast has been reported using central venous access at the groin with a pump system to propel contrast as well as with peripheral intravenous access and use of chest compressions as in cardiopulmonary resuscitation to move the contrast through the body in adults. Potential pitfalls may arise with insufficient contrast volume for patient size or uneven contrast distribution due to blood coagulation within vessels or layering of fluid and contrast simulating vascular filling defects. For this reason, most authors advocate multiple phases of imaging [24, 25, 28, 30, 32] with abnormalities found on more than one phase felt to be true. One unique consideration is that the contrast may alter the chemistry of the intravascular contents and so body fluid sampling should occur prior to PMCTA [26, 27].

Use of PMCTA in infants and children has been described, although the techniques differ somewhat to those utilized in adults (Fig. 18). In one report, vascular access was obtained using the umbilical vessels with administration of 30% water-soluble contrast in 70% water while the body was rotated to improve even contrast distribution. A total of 6 ml (mL) per kilogram (kg) was administered with subsequent spiral CT showing successful vascular and cardiac opacification [33]. A second study described umbilical vascular access with administration of 3–20 mL injections with a scan performed after each. Body and cranial vascular opacification was sufficient to allow identification of an anomaly of the great vessels [34]. A third group found that direct cardiac intraventricular injection of 5–10 mL of contrast was required for adequate chamber visualization, although contrast leakage into the pleural space occurred in a few cases, possibly from cardiac overfilling [35]. Cranial venography performed with sagittal sinus access via the fontanelle has been described by Stein et al. [36] utilizing 25% water-soluble contrast in water with subsequent scanning performed immediately due to rapid venous washout. The amount of contrast was dependent upon patient size. This technique allowed detection of hemorrhage from torn bridging veins. Chevalier et al. [37] performed a modified adult PMCTA technique with central vascular access in a 7-year-old. They used half the volume of an adult technique with one-half the rate of contrast administration and reported successful head and torso vascular opacification. Most recently, Bruch et al. [38] reported that when the umbilical vessels were patent, they could be accessed for PMCTA of the arterial and venous circulations. Intraosseous injection

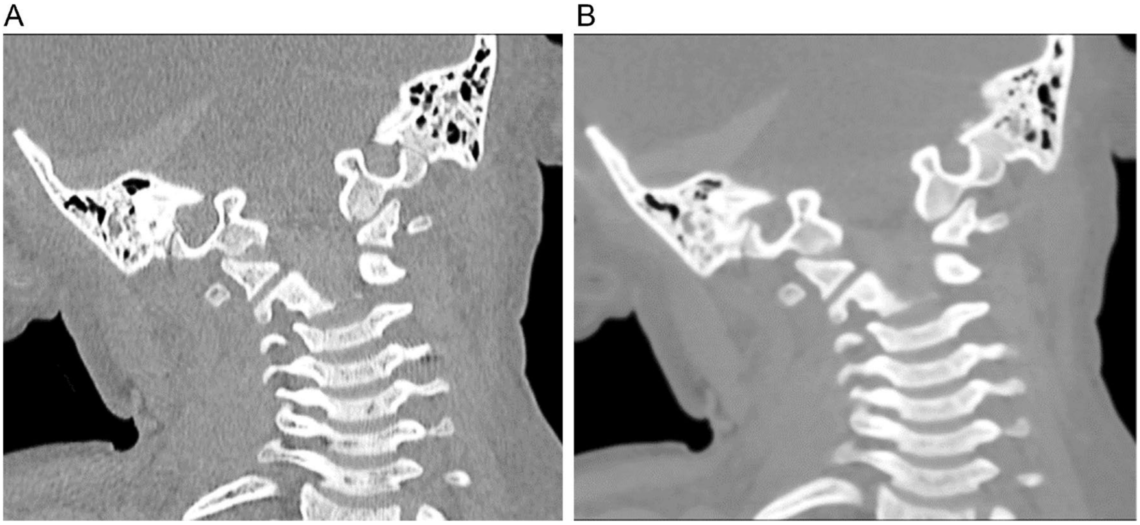

Fig. 11 A 4-year-old boy with unexplained death and circumstances concerning for physical abuse. **a** A 2-mm-thick coronal reformatted image of the cervical spine was reconstructed with a very sharp/bone algorithm and demonstrates trabecular detail. **b** The same coronal reformatted slice reconstructed with a soft tissue algorithm has poor trabecular definition. Both reconstructions are marred by subtle step artifact as the datasets were not reconstructed with overlap

Fig. 12 A 23-day-old boy who succumbed to a respiratory illness. **a** A 2-mm-thick coronal reformatted image shows significant step artifact most noticeable along the right humeral cortex (*arrow*) because the reformatting was created from 2-mm-thick slices with no overlap. **b** The step artifact can be seen in this volume rendered image of the left forearm viewed from an anterior perspective as irregularity of the bone surface (*open arrow*)

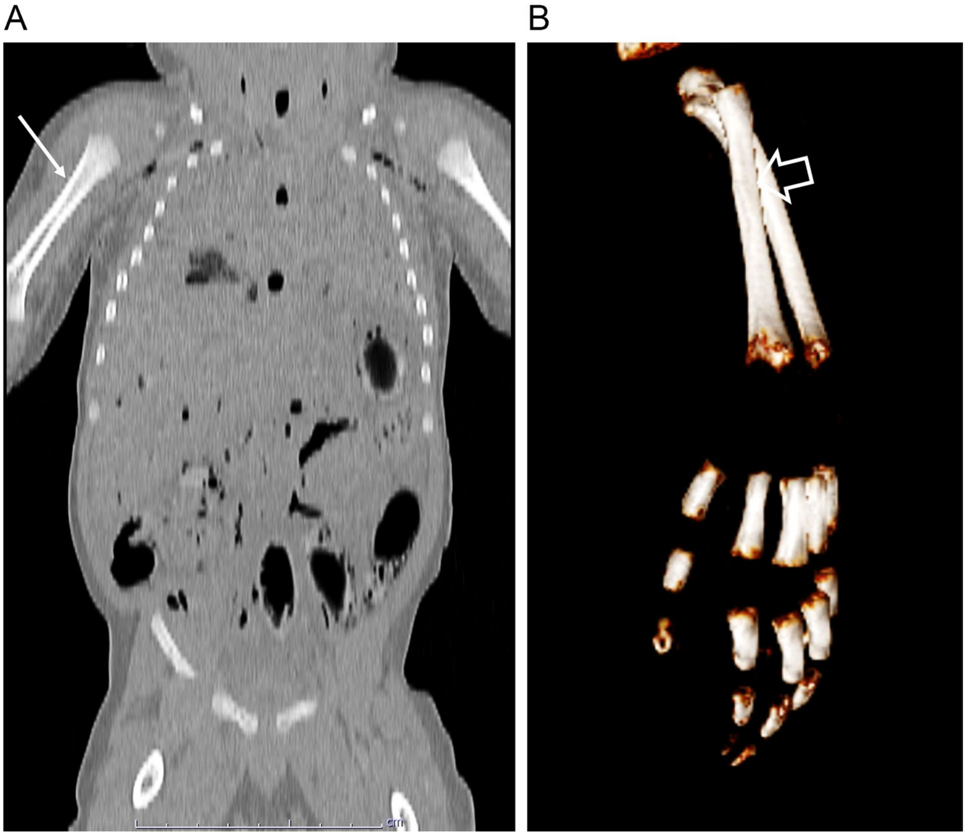

of contrast could also be performed but only opacified the venous circulation unless there was a shunt such as a patent foramen ovale. The femoral vessels could also be accessed for both arterial and venous evaluation in older infants.

Reported scan parameters for PMCTA suggest utilizing a kVp between 110 and 130 [27, 30, 34, 38]; however, a kVp of 100 would be closer to the K-edge of iodine and may improve contrast conspicuity [1, 2]. Other components of

Fig. 13 A 2.5-month-old boy with multiple fractures concerning for physical abuse. **a** A sagittal reconstruction of the humerus created from a dataset with a reconstructed field of view (FOV) of 270 mm and a bone kernel shows irregularity (*white arrows*) at the proximal metaphyseal margin as well as lucency along the zone of provisional calcification (*arrowhead*), but the trabeculae are indistinct. **b** The same sagittal reconstructed slice from a dataset with a reconstructed FOV of 165 mm and the same bone kernel more clearly show the lucency at the zone of provisional calcification (*black arrows*) and the periosteal response at the margins of the metaphysis (*open arrows*). Both datasets are marred by subtle step artifact from non-overlapping slice reconstruction. The green dot at the center of each image is from the post-processing software platform

technique including tube current, pitch, and field of view would be similar to those used for unenhanced PMCT. A soft kernel would likely be most useful. Reconstructions should include maximum intensity projection images, as in routine clinical CTA.

Ventilated PMCT has also been described to try to overcome another postmortem pitfall, that of lung collapse that can obscure lung pathology. Ventilated PMCT attempts to recreate a breath hold by forcing air into the lungs during scanning both opening airways and pushing interstitial fluid back into pulmonary vessels. A pediatric ventilated PMCT technique has been described by Arthurs et al. [39] (Fig. 19). They reported greater success in expanding the lungs and avoiding air leaks resulting in gastric distension utilizing appropriately sized laryngeal mask airways rather than existing endotracheal tubes. Mechanical ventilation with positive end-expiratory pressure sufficient to maintain chest wall height during scanning provided superior lung expansion to ventilation with a bag. The authors recommended scanning before and following artificial ventilation in case of artifactual pneumothorax creation. A multidetector scanner was employed to obtain a continuous spiral acquisition with variable tube current, a kVp of 120, a pitch of 1, and 0.625-mm collimation.

A discussion of microfocus CT is beyond the scope of this article.

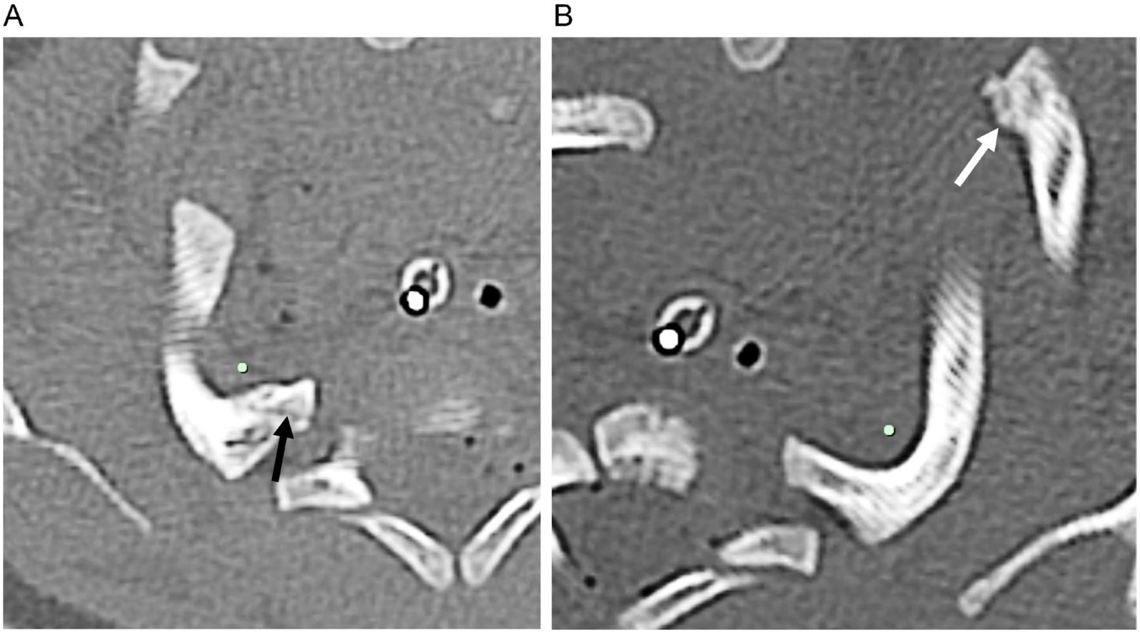

Fig. 14 A 7-week-old girl with unexplained death. **a** A 2-mm-thick oblique axial reconstruction along the posterior right first rib shows a linear fracture of the posterior rib extending into the costovertebral joint (*black arrow*). There is cortical irregularity indicating healing response. **b** An oblique reconstruction along the posterior left first rib shows a normal first rib appearance, but there is a costochondral junction fracture with healing response at the anterior left 2nd rib (*white arrow*). Both images are marred by reconstruction from non-overlapping slices. The green dots within both images are a localizer tool in the post-processing software used to create these reconstructions

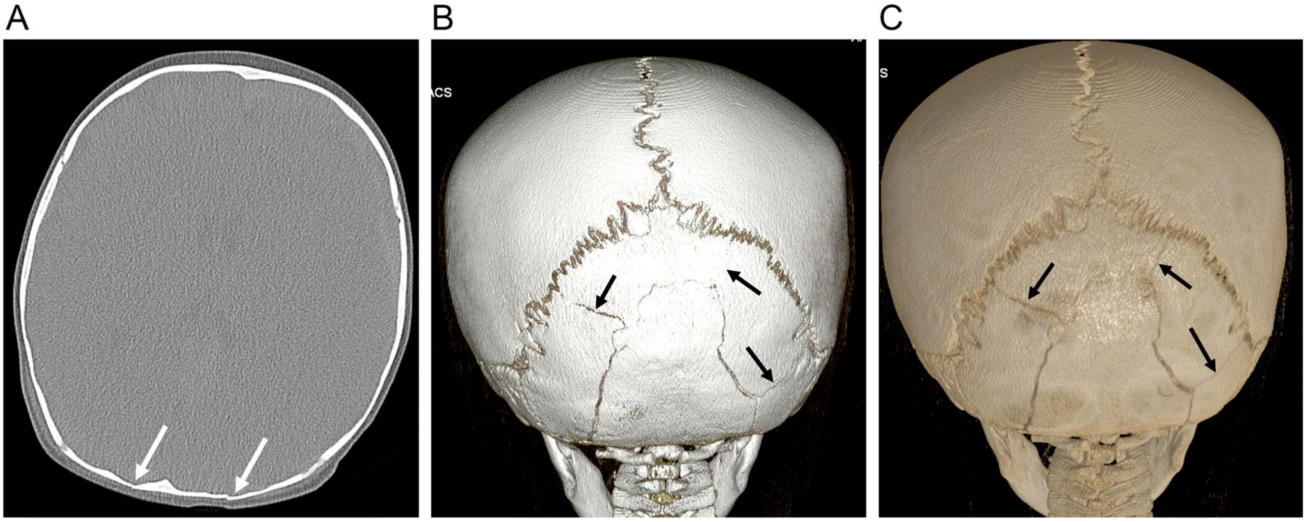

Fig. 15 A 7-month-old boy found unresponsive in a different room from where the parent left him. **a** A 2-mm-thick axial image of the head reconstructed with a bone algorithm shows bilateral occipital fractures (*white arrows*). **b** The complex occipital bone fracture is more apparent on this posterior view 3-dimnesional volume rendered (3-DVR) image (*black arrows*). **c** This cinematic rendering created from the same scan and data as **b** from the same posterior perspective shows the complexity of the fracture more clearly than the 3-DVR image

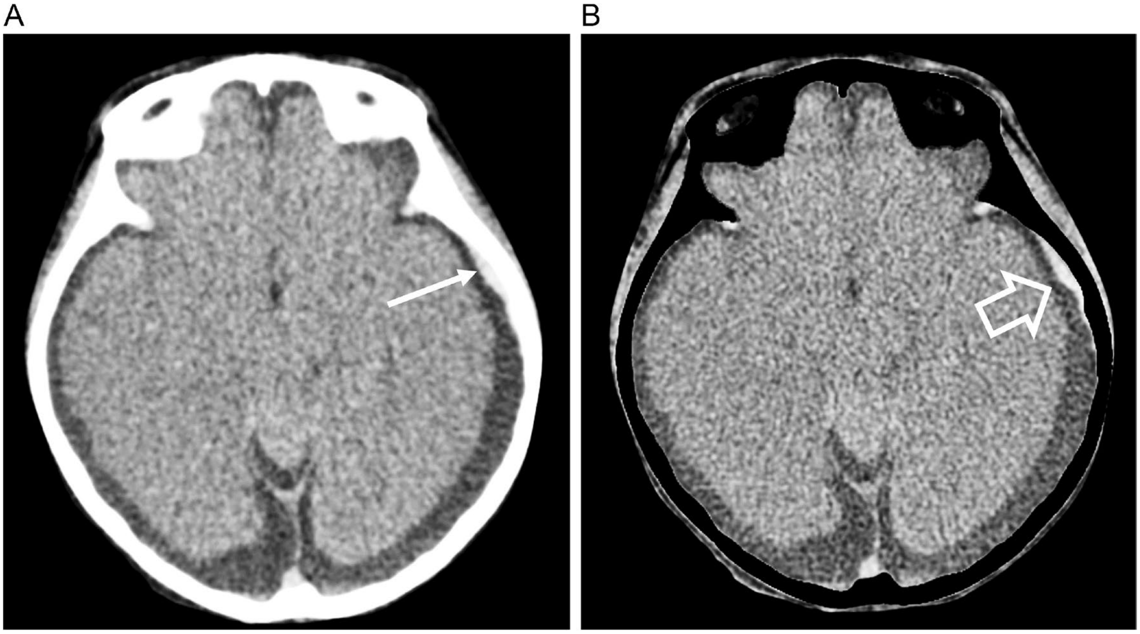

Fig. 16 A 4-year-old girl who died following cardiac arrest. **a** A 3-mm axial image from a dual-energy computed tomography scan (dual source with tube voltage values of 80 and 140 kVp with a tin filter) shows prominent extra axial spaces, a stable finding for this patient, with a small extra axial blood collection on the left (*arrow*). **b** The same slice reconstructed with spectral decomposition to select voxels with calcium shows virtual "bone removal" with resulting increased conspicuity of the extra axial collection (*open arrow*) confirmed to be a small subdural hematoma at autopsy

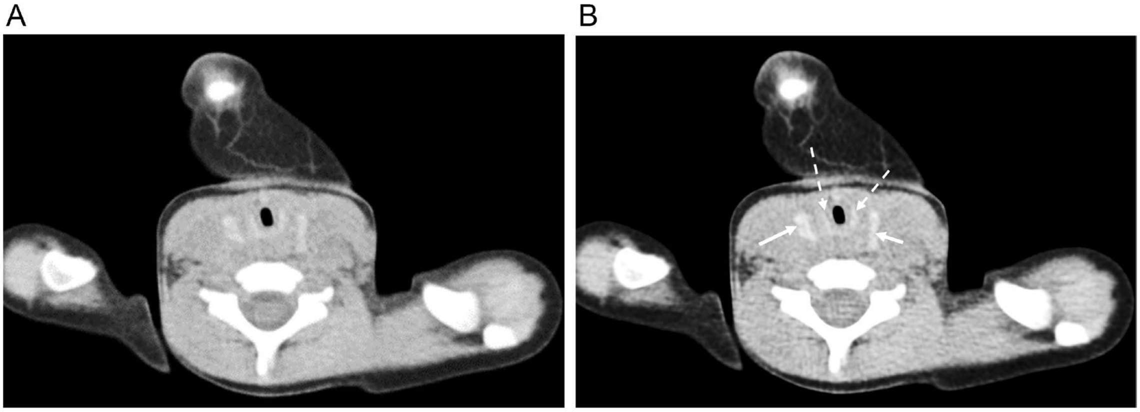

Fig. 17 A 20-month-old girl with a complex medical condition found unresponsive in bed. **a** A 3-mm thick axial image was created from a dual-energy acquisition: dual source with kVp values of 80 and 140 with a tin filter was reconstructed as though the beam consisted only of 70 kV photons, similar to the average energy of 120 kVp technique. There is mild image noise and somewhat limited soft tissue differentiation. **b** The same image was created as if the beam energy was monoenergetic at 55 kV, closer to the K-edge of iodine. There is mildly improved soft tissue differentiation, particularly at the thyroid gland (*white arrows*) and arytenoid cartilage (*dashed arrows*), but at the expense of slightly increased image noise. This type of reconstruction may prove useful for soft tissue evaluation, but more work is needed to assess the impact of multienergy imaging on postmortem computed tomography

Segmentation and related applications

A discussion of segmentation techniques is beyond the scope of this article and the reader is referred to the excellent discussion by Ebert et al. [14] for further information. A clear, artifact-free, high-resolution dataset is required for optimal segmentation. A number of segmentation techniques are available for selection of desired structures. The most common techniques are thresholding, using a set range of attenuation values to select the appropriate

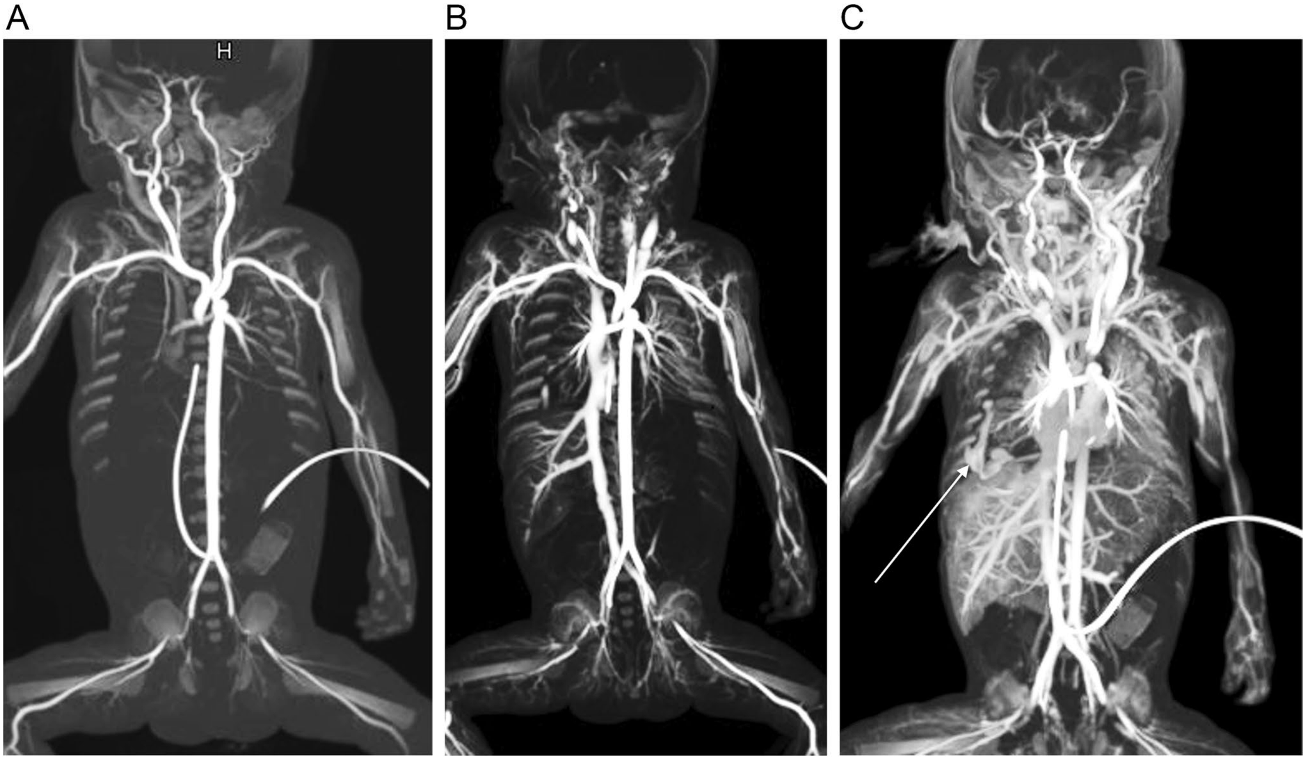

Fig. 18 A 2-day-old premature girl of 700 g who developed acute onset respiratory insufficiency requiring cardiopulmonary resuscitation that was unsuccessful. There was a large amount of fresh blood from the mouth and nose, suspected to be due to pulmonary hemorrhage. The parents consented to postmortem imaging but not autopsy. Computed tomography angiography was performed. An initial unenhanced scan without contrast was performed (not shown). **a** Coronal maximum intensity projection (MIP) image obtained 1 min after 5 mL iodinated contrast through the arterial line in the right arm with an injection rate of approximately 0.3 mL per second. **b** Coronal MIP image obtained 1 min after 3 mL iodinated contrast was administered through the venous umbilical line with a gentle injection rate of about 0.5 mL/s. **c** Coronal MIP image obtained in a late phase more than 5 min after the venous injection. The images demonstrate normal arterial and venous anatomy with venous contrast extravasation (*arrow*) from the right lower lobe into the right pleural space

anatomy, and region growing, using a selected point to extend the region of interest to neighboring voxels with similar attenuation values [14]. Thresholding is best utilized for structures such as bone, metal, or air that differ greatly in attenuation from surrounding structures. Region growing works well with smaller structures or to refine a structure selected by thresholding. Once the desired anatomy is carefully selected, the data can be utilized for volumetry [14] or converted to a polygon mesh as a stereolithography file [14]. The next step is repair of any holes or overlaps in the mesh, reduction of the number of triangles, smoothing, and fragment removal. At this point, the file can be converted to a portable document format for display, 3-D printed, or utilized in virtual reality or augmented reality applications [14]. This type of data manipulation can be very effective for teaching and courtroom display, but because the data has been technically manipulated, volume renderings and 3-D prints are used for demonstration and are not considered evidence.

Summary

PMCT can be a useful tool in death investigation in children, both in the setting of perinatal demise and in forensic investigation. Unlike clinical CT performed for living patients, scanning protocols can be adjusted to provide high-resolution, low-noise datasets. Multiple scans can be performed, if necessary, based on patient size and/or positioning, or in the setting of high-attenuation material or objects. Advances in data processing allow multiplanar reformatting to allow optimal visibility of pathology, volume rendering for surface analysis and spatial relationships, and even spectral decomposition in the setting of dual-energy or photon counting CT. Stored data can be reconstructed or even printed at a later date for education or legal presentation, but to be able to utilize the data, optimal technique in acquiring the scan is key.

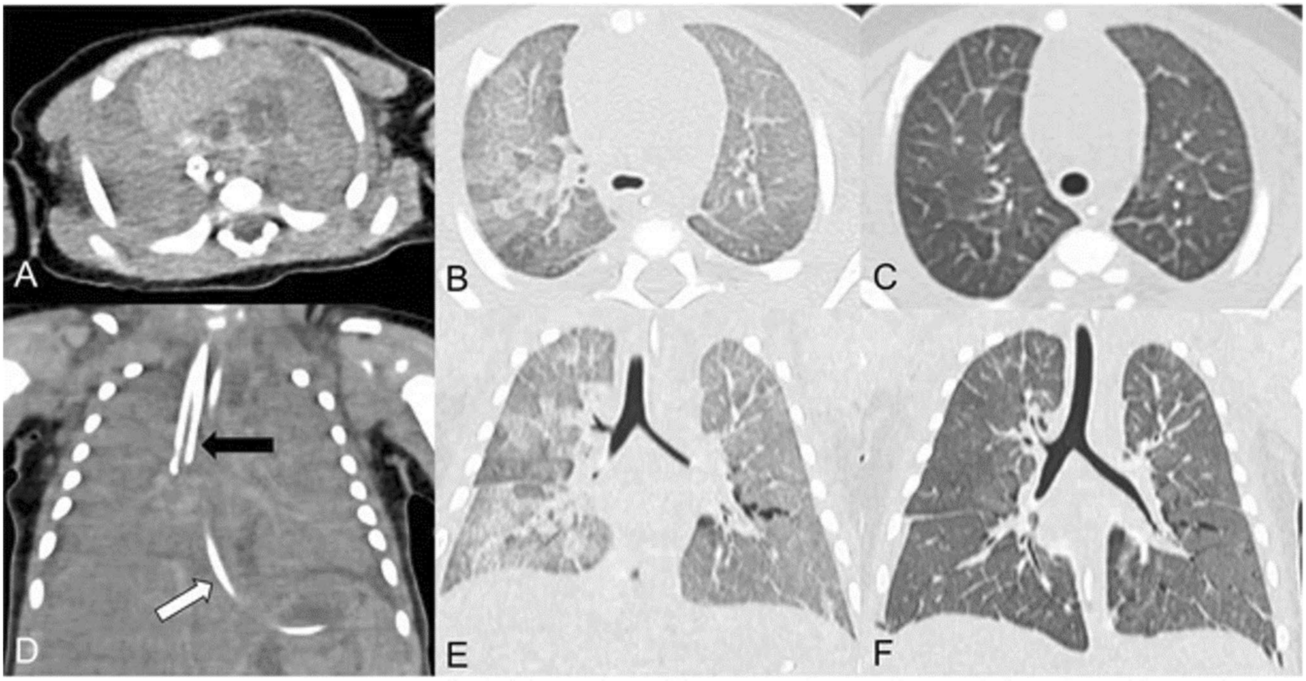

Fig. 19 Ventilated postmortem computed tomography scan in a 28-day-old infant. Axial (**a**–**c**) and coronal (**d**–**f**) reformatted images are shown before ventilation (**a**, **d**), with the endotracheal tube tip in the right main bronchus (*black arrow*), after manual bag ventilation following endotracheal tube removal (**b**, **e**), and after mechanical positive end-expiratory pressure ventilation (**c**, **f**). A nasogastric tube is also demonstrated (*white arrow*) on the initial phase and was removed prior to subsequent scans. Reproduced with permission from Arthurs OJ, Guy A, Kiho L, Sebire NJ. Ventilated postmortem computed tomography in children: feasibility and initial experience. *Int J Legal Med*. 2015;129(5):1113–20

Author contribution S.W.G. interpreted and collected some of the cases, organized and wrote the manuscript, and collected references. M.H. interpreted and collected most of the cases and provided input into manuscript design. Both authors reviewed and approved the final manuscript.

Declarations

Conflicts of interest None.

References

1. Flach PM, Gascho D, Schweitzer W, Ruder TD, Berger N, Ross SG et al (2014) Imaging in forensic radiology: an illustrated guide for postmortem computed tomography technique and protocols. Forensic Sci Med Pathol 10:583–606. https://doi.org/10.1007/s12024-014-9555-6
2. Gascho D, Thali MJ, Niemann T (2018) Post-mortem computed tomography: technical principles and recommended parameter settings for high resolution imaging. Med Sci Law 58:70–82. https://doi.org/10.1177/0025802417747167
3. Norberti N, Tonelli P, Giaconi C, Nardi C, Focardi M, Nesi G et al (2019) State of the art in post-mortem computed tomography: a review of the literature. Virchows Arch 475:139–150. https://doi.org/10.1007/s00428-019-02562-4
4. Gould SW, Harty MP, Givler NE, Christensen TE, Curtin RN, Harcke HT (2019) Pediatric postmortem computed tomography: initial experience at a children's hospital in the United States. Pediatr Radiol 49:1113–1129. https://doi.org/10.1007/s00247-019-04433-1
5. Shelmerdine SC, Gerrard CY, Rao P, Lynch M, Kroll J, Martin D et al (2019) Joint European Society of Paediatric Radiology (ESPR) and International Society for Forensic Radiology and Imaging (ISFRI) guidelines: paediatric postmortem computed tomography imaging protocol. Pediatr Radiol 49:694–701. https://doi.org/10.1007/s00247-018-04340-x
6. Ford JM, Decker SJ (2016) Computed tomography slice thickness and its effects on three-dimensional reconstruction of anatomical structures. J Forens Radiol Imaging 4:43–46. https://doi.org/10.1016/j.jofri.2015.10.004
7. Shelmerdine SC, Davendralingam N, Langan D, Palm L, Mangham C, Arthurs OJ, and CORNRD Study Collaborators (2024) Post-mortem skeletal survey (PMSS) versus post-mortem computed tomography (PMCT) for the detection of corner metaphyseal lesions (CML) in children. EurRadiol. https://doi.org/10.1007/s00330-024-10679-7
8. Eilfritz J, Jarell SJ (2023) "Developments in postmortem imaging" in Ely SF and Gill JR (eds) Principles of Forensic Pathology, Elsevier, Amsterdam
9. Mahesh M (2002) The AAPM/RSNA physics tutorial for residents: search for isotropic resolution in CT from conventional through multiple-row detector. Radiographics 22:949–962. https://doi.org/10.1148/radiographics.22.4.g02jl14949
10. Edwards H, Shelmerdine SC, Arthurs OJ (2023) Forensic postmortem CT in children. Clin Radiol 78:839–847. https://doi.org/10.1016/j.crad.2023.06.001
11. Speelman AC, Engel-Hills PC, Martin LJ, van Rijn RR, Offiah AC (2022) Postmortem computed tomography plus forensic autopsy

for determining the cause of death in child fatalities. Pediatr Radiol 52:2620–2629. https://doi.org/10.1007/s00247-022-05406-7

12. Cheung JP, Shugard E, Mistry N, Poullot J, Chen J (2018) Evaluating the impact of extended field-of view CT reconstructions on CT values and dosimetric accuracy in radiation therapy. Med Phys 46:892–901. https://doi.org/10.1002/mp.13299
13. Barrett JF, Keat N (2004) Artifacts in CT: recognition and avoidance. Radiographics 24:1679–1691. https://doi.org/10.1148/rg.246045065
14. Ebert LC, Dobay A, Franckenberg S, Thali MJ, Decker S, Ford J (2022) Image segmentation of post-mortem computed tomography data in forensic imaging: methods and applications. Forens Imag 28:200483. https://doi.org/10.1016/j.fri.2021.200483
15. Ebert LC, Franckenberg S, Sieberth T, Schweitzer W, Thali M, Ford J, Decker S (2021) A review of visualization techniques of post-mortem computed tomography data for forensic death investigations. Int J Legal Med 135:1855–1867. https://doi.org/10.1007/s00414-021-02581-4
16. Yang KM, Lynch M (2011) O'Donnell C (2011) "Buckle" rib fracture: an artifact following cardio-pulmonary resuscitation detected on post-mortem CT. Legal Med 13:233–239. https://doi.org/10.1016/j.legalmed.2011.05.004
17. Brough AL, Rutty GN, Black S, Morgan B (2012) Post-mortem computed tomography and 3-D imaging: anthropological applications for juvenile remains. Forens Sci Med Pathol 8:270–279. https://doi.org/10.1007/s12024-012-9344-z
18. Orman G, Wagner M, Seeburg D, Zamora C, Oshmyansky A, Tekes A et al (2015) Pediatric skull fracture diagnosis: should 3-D CT reconstructions be added as routine imaging? J Neurosurg Pediatr 16:426–431. https://doi.org/10.3171/2015.3.PEDS1553
19. Shelmerdine SC, Sebire NJ, Calder AD, Arthurs OJ (2021) 3-D cinematic rendering of fetal skeletal dysplasias using postmortem computed tomography. Ultrasound Obstet Gynecol 57:659–660. https://doi.org/10.1002/uog.23140
20. Dappa E, Higashigaito K, Fornaro J, Leschka S, Wildermuth S, Alkadhi H (2016) Cinematic rendering-an alternative to volume rendering for 3-D computed tomographic imaging. Insights Imaging 7:849–856. https://doi.org/10.1007/s13244-016-0518-1
21. Eid M, DeCecco CN, Nance JW, Caruso D, Albrecht MH, Spandorfer AJ, De Santis D, Varga-Szemes A (2017) Schoepf UJ (2017) Cinematic rendering in CT: a novel, lifelike 3-D visualization technique. Am J Roentgen 209:370–379. https://doi.org/10.2214/AJR.17.17850
22. Persson A, Jackowski C, Engstrom E, Zachrisson H (2008) Advances of dual source, dual-energy imaging in post-mortem CT. Eur J Radiol 68:446–455. https://doi.org/10.1016/j.ejrad.2008.05.008
23. Rajiah P, Parakh A, Kay F, Baruah D, Kambadakone AR, Leng S (2020) Update on multienergy CT: physics, principles, and applications. Radiographics 40:1284–1308. https://doi.org/10.1148/rg.2020200038
24. Chandy PE, Murray N, Khasanova E, Nasir MU, Nicolau S, Macri F (2020) Postmortem CT in trauma: an overview. Can Assoc of Radiol J 71:403–414. https://doi.org/10.1177/0846537120909503
25. Busardo FP, Frati P, Guglielmi G, Grilli G, Pinto A, Rotondo A et al (2015) Postmortem-computed tomography and postmortem-computed tomography-angiography: a focused update. Radiol Med 120:810–823. https://doi.org/10.1007/s11547-015-0559-4
26. Lee H, Lee S, Cha JG, Baek T, Yang K (2019) Postmortem computed tomography and computed tomography angiography. J Thoracic Imaging 34:286–298. https://doi.org/10.1097/RTI.0000000000000398
27. Grabherr S, Doenz F, Steger B, Dirnhofer R, Dominguez A, Solberger B et al (2011) Multi-phase post-mortem CT angiography: development of a standardized protocol. Int J Legal Med 125:791–802. https://doi.org/10.1007/s00414-010-0526-5
28. Grabherr S, Grimm J, Dominguez A, Vanhaebost J, Mangin P (2014) Advances in post-mortem CT-angiography. Br J Radiol 87:20130488. https://doi.org/10.1259/bjr.20130488
29. Jackowski C, Bollinger S, Aghayev E, Christe A, Kilchoer T, Aebi B et al (2006) Reduction of postmortem angiography-induced tissue edema by using polyethylene glycol as a contrast agent dissolver. J Forens Sci 51:1134–1137. https://doi.org/10.1111/j.1556-4029.2006.00207.x
30. Ross S, Spendlove D, Bollinger S, Christie A, Oesterhelweg L, Grabherr S et al (2008) Postmortem whole-body CT angiography: evaluation of two contrast media solutions. Am J Roentgenol 190:1380–1389. https://doi.org/10.2214/AJR.07.3082
31. Ross SG, Bolliger SA, Ampanozi G, Oesterhelweg L, Thali MJ, Flach PM (2014) Postmortem CT angiography: capabilites and limitations in traumatic and natural causes of death. Radiographics 34:830–846. https://doi.org/10.1148/rg.343115169
32. Grabherr S, Egger C, Vilarino R, Campana L, Jotterand M, Dedouit F (2017) Modern post-mortem imaging: an update on recent developments. For Sci Res 2:52–64. https://doi.org/10.1080/20961790.2017.1330738
33. Sarda-Quarello L, Bartoli C, Laurent P-E, Torrents J, Piercecchi-Marti M-D, Sigaudy S et al (2016) Whole body perinatal postmortem angiography. Diagn Interv Imaging 97:121–124. https://doi.org/10.1016/j.diii.2014.11.002
34. Wozniak KJ, Moskala A, Kluza P, Romaszko K, Lopatin O, Rzepecka-Wozniak E (2015) Whole-body post-mortem computed tomography angiography of a newborn revealing transposition of great arteries. Int J Legal Med 129:1253–1258. https://doi.org/10.1007/s00414-015-1267-2
35. Votino C, Cannie M, Segers V, Dobrescu O, Dessy H, Gallo V et al (2012) Virtual autopsy by computed tomographic angiography of the fetal heart: a feasibility study. Ultrasound Obstet Gynecol 39:679–84. https://doi.org/10.1002/uog.11150
36. Stein KM, Ruf K, Ganten MK, Mattern R (2006) Representation of cerebral bridging veins in infants by postmortem computed tomography. For Sci Int 163:93–101. https://doi.org/10.1016/j.forsciint.2005.11.015
37. Chevalier C, Michaud K, Palmiere C, Alamo L, Mangin P, Grabherr S (2015) Multiphase postmortem computed tomography angiography in pediatrics: a case report. Am J Forensic Med Pathol 36:239–244. https://doi.org/10.1097/PAF.0000000000000189
38. Bruch GM, Hofer P, Ferraz da Silva LF, Pires-Davidson JR, Bentos dos Santos GA, Fischer FT (2023) Pediatric postmortem CT angiography: validation of vascular access for PMCT angiography in stillbirths, babies, and toddlers. Forensic Sci Med Pathol. https://doi.org/10.1007/s12024-023-00726-y
39. Arthurs OJ, Guy A, Kiho L, Sebire NJ (2015) Ventilated post mortem computed tomography in children: feasibility and initial experience. Int J Legal Med 129:1113–1120. https://doi.org/10.1007/s00414-015-1189-z